Journal of Nuclear Medicine, published on April 16, 2021 as doi:10.2967/jnumed.120.254961

Direct comparison of the tau PET tracers [^{18}F]flortaucipir and [^{18}F]MK-6240 in human subjects

Alexandra Gogola[1], Davneet S. Minhas[1], Victor L. Villemagne[2], Ann D. Cohen[2], James M. Mountz[1], Tharick A. Pascoal[2], Charles M. Laymon[1,3], N. Scott Mason[1], Milos D. Ikonomovic[2,4], Chester A. Mathis[1], Beth E. Snitz[4], Oscar L. Lopez[4], William E. Klunk[2], and Brian J. Lopresti[1]

Departments of [1]Radiology. [2]Psychiatry, [3]Bioengineering and [4]Neurology, University of Pittsburgh, Pittsburgh, PA, USA

Corresponding Author:
Brian J. Lopresti
PET Facility, B-938 PUH
200 Lothrop St.
Pittsburgh, PA 15213
Tel: (412)647-0736 (office)
(412)977-6196 (mobile)
Email: BrianL@pitt.edu

First Author:
Alexandra Gogola
PET Facility, B-938 PUH
200 Lothrop St.
Pittsburgh, PA 15213
Tel: (412)647-0736 (office)
(319)830-4579 (mobile)
Email: judischal@upmc.edu

Word Count: 5,959 (all inclusive)

Financial Support: National Institute on Aging grants AG025204 and AG005133

Running Title : COMPARING FLORTAUCIPIR AND MK-6240 PET

ABSTRACT

Tau PET tracers exhibit varying levels of specific signal and distinct off-target binding patterns that are more diverse than amyloid PET tracers. This study compares two frequently used tau PET tracers, [^{18}F]flortaucipir (FTP) and [^{18}F]MK-6240, in the same subjects. **METHODS:** [^{18}F]flortaucipir and [^{18}F]MK-6240 scans were collected within two months in 15 elderly subjects varying in terms of clinical diagnosis and cognition. FreeSurfer v5.3 was applied to 3T MR images to segment Braak pathologic regions (I-VI) for PET analyses. Off-target binding was assessed in choroid plexus, meninges, and striatum. SUVR outcomes were determined over 80-100 min ([^{18}F]flortaucipir) or 70-90 min ([^{18}F]MK-6240) normalized to cerebellar grey matter. Blinded visual interpretation of images was performed by five raters for both medial temporal lobe (MTL) and neocortex (NEO) and an overall (majority) rating determined. **RESULTS:** Overall visual ratings showed complete concordance between radiotracers for both MTL and NEO. SUVR outcomes were highly correlated (r^2>0.92; p << 0.001) for all Braak regions except Braak II. The dynamic range of SUVR values in target regions was approximately two-fold higher for [^{18}F]MK-6240 compared to [^{18}F]flortaucipir. Cerebellar SUV values were similar for [^{18}F]MK-6240 and [^{18}F]flortaucipir, suggesting that differences in SUVR values are driven by specific signal. Apparent off-target binding in striatum and choroid plexus was often observed with [^{18}F]flortaucipir, and most often in meninges with [^{18}F]MK-6240. **CONCLUSION:** Both [^{18}F]MK-6240 and [^{18}F]flortaucipir are capable of quantifying signal in a common set of brain regions that develop tau pathology in AD and perform equally well in visual interpretations. Each also shows distinct patterns of apparent off-target binding. [^{18}F]MK-6240 showed greater dynamic range in SUVR estimates, which may be an advantage for detecting very early signal or in longitudinal studies designed to detect small interval changes.

Keywords: Tau, PET, Alzheimer's disease, [^{18}F]flortaucipir, [^{18}F]MK-6240

DISCLOSURE

GE Healthcare holds a license agreement with the University of Pittsburgh based on some of the technology described in this manuscript. Drs. William E. Klunk and Chester A. Mathis are co-inventors of PiB and, as such, have a financial interest in this license agreement. Dr. Ikonomovic received research funding from GE Healthcare.

INTRODUCTION

Alzheimer disease (AD) is pathologically characterized by two specific brain pathologies: extracellular beta-amyloid (Aβ) plaques and intracellular neurofibrillary tangles (NFTs) comprised of hyperphosphorylated tau protein. Although much evidence supports the amyloid cascade hypothesis of AD (*1*), whereby abnormal Aβ deposition is an initiating feature of AD, tau pathology is more closely linked to symptom severity, rate of decline and development of dementia in AD pathophysiological spectrum patients (*2*), and decline of visuospatial and language functions (*3*).

The ability to detect tau pathology in the living brain is critical for understanding the relationship between neuropathology and clinical symptoms and monitoring the efficacy of novel anti-tau therapies (*3-7*). In addition to recently U.S Food and Drug Administration (FDA)-approved flortaucipir (TAUVID™), previously known as [^{18}F]AV-1451 and [^{18}F]T807 (*8*), several tau radioligands have been advanced to investigational human studies including [^{18}F]MK-6240 (*9*), [^{18}F]THK-5317, [^{18}F]THK-5351, [^{11}C]PBB3, [^{18}F]RO-948, [^{18}F]PI-2620, [^{18}F]GTP1, and [^{18}F]PM-PBB3 (*4*). Ongoing investigations underscore that tau radioligands differ in terms of specificity to species of tau aggregates, dynamic range, non-specific and off-target binding (*4*). Of the tau imaging agents under development, [^{18}F]flortaucipir and [^{18}F]MK-6240 have seen widespread investigational use and have emerged as leading candidates for clinical translation.

Flortaucipir shows high in vitro binding affinity and selectivity for paired helical filament tau (PHF-tau) constituting NFT pathology, and in vivo indices of tau load correlate well with post-mortem AD-related tau pathology (*10*). In vivo patterns of [^{18}F]flortaucipir retention reflect Braak pathological staging (*11*) and support PET-based staging of AD (*6*). Robust [^{18}F]flortaucipir in vivo signal is observed predominantly in patients who show AD-characteristic Aβ deposits (*4*). Data suggest that [^{18}F]flortaucipir is specific for the mixed 3- and 4-repeat

(3R/4R) PHF-tau deposits prevalent in AD NFTs and dystrophic neurites (*4*), and suggest utility for differential diagnoses of AD from other tauopathies (*12*).

An autopsy confirmation study of [^{18}F]flortaucipir detected an advanced level of NFT pathology (Braak V-VI) and high levels of neuropathologic change according to the joint National Institute of Aging-Alzheimer's Association criteria for AD neuropathologic diagnosis (*10*). However, some [^{18}F]flortaucipir characteristics are not ideal for PET imaging assessments, such as slower clearance from cortex, with respect to the cerebellum, with increasing tau pathologic burden, resulting in unstable standard uptake value ratio (SUVR) outcomes even after long periods (*13*). Off-target binding in basal ganglia, choroid plexus, and other regions (*4*) may influence specific signal determination in adjacent regions. Although the test-retest reproducibility of [^{18}F]flortaucipir is excellent (<4%)(*14*), low signal in mild cognitive impairment (MCI) and early AD combined with high non-specific retention in amyloid-negative controls may pose challenges for early detection and tracking tau aggregation longitudinally (*15,16*).

[^{18}F]MK-6240 has also shown high affinity and selectivity for 3R/4R PHF-tau (*5,17*) and has advanced to human studies (*4,18*). In amyloid PET-positive subjects, [^{18}F]MK-6240 showed excellent brain uptake and retention patterns consistent with Braak stages of tau pathology (*4,18*). Like [^{18}F]flortaucipir, the slowly equilibrating kinetics of [^{18}F]MK-6240 may represent a source of bias in SUVR outcomes for typical scanning intervals (e.g.; 70-90 min, 90-110 min) (*5,17-21*). Off-target binding of [^{18}F]MK-6240 is absent in basal ganglia and choroid plexus (*17,18,21*), although off-target binding in the retina, ethmoid sinus, substantia nigra, and dura mater is common (*19*). In vivo studies of [^{18}F]MK-6240 show good reproducibility (test-retest < 6 %)(*18,22*), an ability to differentiate cognitively normal from MCI/AD patients (*19,23*), and sensitivity for detecting tau in early disease stages (*21*).

While amyloid-PET tracers show very similar patterns of specific signal across subjects and radiotracers, this is not the case for tau tracers. Although both [^{18}F]flortaucipir and [^{18}F]MK-

6240 appear to detect tau deposits in vivo, evaluating the relative performance of these two radiotracers is complicated by the absence of direct comparisons performed in the same subjects. This shortcoming layers biological variability on top of tracer variability since there is a wide range of spatial distribution and severity of tau pathology across individuals (*3*). The present work describes a direct comparison of [^{18}F]flortaucipir and [^{18}F]MK-6240 in a group of 15 subjects having a range of clinical diagnoses studied with both radiotracers within a two-month interval.

MATERIALS AND METHODS

Human Subjects

The study was approved by the University of Pittsburgh's Institutional Review Board and all subjects or their caregivers provided consent for the Alzheimer's Disease Research Center (ADRC) examination and imaging protocol. 15 subjects were recruited through the University of Pittsburgh ADRC and other population-based studies (Table 1), selected to represent a range of AD pathologic burden based on cognition and amyloid PET. No subjects were excluded. All subjects underwent a battery of cognitive tests and consensus clinical diagnosis performed by the same ADRC neurologist (OLL), geriatric psychiatrist (WEK), and neuropsychologist (BES) (*24*). A [^{11}C]PiB scan was performed on the day of the [^{18}F]flortaucipir scan to determine amyloid status. Five subjects were clinically diagnosed with probable AD (MMSE range 9 – 29) and all were globally PiB positive. One subject was classified as MCI-amnestic (MMSE=22), but a negative [^{11}C]PiB scan suggested a non-AD etiology. The remaining 9 subjects had no subjective cognitive complaint (NC), although six scored outside of normal ranges on at least one objective measure of cognition, memory, or executive function (classified as 'impaired test without complaints'). Among the 9 NC subjects, 7/9 had MMSE scores within normal ranges (28-30) and only one NC subject was globally PiB positive.

Imaging

[^{11}C]PiB and [^{18}F]MK-6240 were produced in accordance with Drug Master Files approved by the University of Pittsburgh Radioactive Drug Research Committee (RDRC). Precursors for [^{18}F]flortaucipir and [^{18}F]MK-6240 were provided by Avid Radiopharmaceuticals, Inc. and Cerveau Technologies, Inc. under existing agreements. [^{18}F]flortaucipir was prepared in accordance with procedures detailed in FDA-approved IND #123396 and [^{18}F]MK-6240 as previously described(*9*). [^{18}F]flortaucipir (340±19 MBq MBq) and [^{18}F]MK-6240 PET scans (189±15 MBq) PET scans were collected within 26±14 days (max: 54 days) on a Siemens Biograph mCT (TrueV) (Siemens Healthcare, Erlangen, Germany) and reconstructed as previously described (*25*). To assess amyloid status, [^{11}C]PiB scans (50-70 minutes, 529±107 MBq) were collected on a Siemens ECAT HR+ on the same day as [^{18}F]flortaucipir scans (*26*). A sagittal T1-weighted MPRAGE MR image was acquired using a 3.0T Siemens PRISMA scanner (Siemens Healthcare, Erlangen, Germany) for brain segmentation and parcellation.

Data Analysis

MR images were processed using FreeSurfer v5.3 to obtain a brain parcellation atlas for PET image sampling as previously described (*25,27*). Briefly, motion-corrected [^{18}F]MK-6240 and [^{18}F]flortaucipir images were summed over 70-90 minutes for [^{18}F]MK-6240 (*21*) and 80-100 minutes for [^{18}F]flortaucipir (*13,28*) and registered to a subject-specific reference MR image. The FreeSurfer parcellation template was used to sample summed PET images, and a volume-weighted average of FreeSurfer regions was calculated for each of six composite Braak stage regions-of-interest (ROI) (*11*) (**Error! Reference source not found.**, Supplemental Table 1). Striatal FreeSurfer ROIs (caudate, putamen, accumbens, pallidum) were excluded from the composite Braak V ROI due to frequent off-target binding of [^{18}F]flortaucipir, but examined separately as a composite striatal region (bilateral), along with the choroid plexus (unilateral due

to asymmetries) and meninges, to assess off-target binding (*5*). Regional [^{18}F]flortaucipir and [^{18}F]MK-6240 SUVR values and SUVR images were calculated using cerebellar grey matter as reference (*19,29*).

To compare off-target binding in meninges individual MR images were normalized into MNI space using SPM12 software (Statistical Parametric Mapping, University College, London). The c4 ROI (meninges+bone) was extracted from SPM12's tissue probability map and edited to exclude other head and neck tissues based on an average MR of all 15 subjects (Supplementary Figure 1). The c4 ROI was subsequently transformed back to native space for PET image sampling. Voxel-wise comparisons of [^{18}F]flortaucipir and [^{18}F]MK-6240 SUVR images were performed using SPM12. T-value parametric maps (representing voxels where [^{18}F]MK-6240 > [^{18}F]flortaucipir and [^{18}F]flortaucipir > [^{18}F]MK-6240) were generated from the output of the paired t-test and overlaid on an MRI template for visualization.

Visual Assessments

Visual assessments of [^{18}F]flortaucipir and [^{18}F]MK-6240 SUVR images were performed by five experienced raters using a randomized coding scheme. Ratings were performed using only the PET images, which were assessed for tau pathology in medial temporal lobe (MTL) and neocortex (NEO). Interrater reliability (Fleiss' kappa, κ) was assessed across tracers and regions. Overall MTL and NEO ratings for assessing radiotracer concordance were based on a simple majority of five individual ratings. Additional details are provided in the supplement.

RESULTS

PET Imaging

[^{18}F]flortaucipir and [^{18}F]MK-6240 PET SUVR images displayed a range of tau pathology, with patterns of cortical involvement that were primarily posterior (AD2, AD3), highly focal (AD1), or

widespread (AD4) (Figure 2). In NC subjects, tau PET signal for both radiotracers was modest and most prominent in the MTL.

Visual Assessments

Five raters assessed abnormal tracer retention in MTL and NEO for [^{18}F]flortaucipir and [^{18}F]MK-6240. Overall tau-positivity ratings showed complete concordance between radiotracers for MTL and NEO (Table 2), and there was substantial agreement between raters ($\kappa > 0.73$) for both regions (MTL and NEO) and radiotracers (Table 3). Individual ratings showed complete agreement for all AD subjects and were least reliable in cases with low levels of tau pathology (e.g. NC4 and NC5, Supplementary Figure 2).

SUVR Analyses

[^{18}F]flortaucipir and [^{18}F]MK-6240 SUVR values were highly correlated ($r^2 > 0.9$; $p << 0.001$) across Braak stage regions (Figure 3) except for Braak II ($r^2 = 0.52$; $p=0.0024$). However, the dynamic range ($SUVR_{max} – SUVR_{min}$) of SUVR, as indicated by the regression slope, was approximately two-fold greater for [^{18}F]MK-6240 across Braak stage regions except Braak II, where the difference was more modest (1.4x). The distributions of cerebellar grey matter standardized uptake values (SUV_{cer}) were not significantly different between [^{18}F]flortaucipir and [^{18}F]MK-6240 ($p > 0.4$, paired t-test), with a mean SUV_{cer} of 0.88 ± 0.18 and 0.84 ± 0.16, respectively (Figure 3, right).

Off-Target Binding

Figure 4 shows the distribution of SUVR outcomes and representative images of typical off-target binding, where striatum and choroid plexus are frequent loci of [^{18}F]flortaucipir off-target signal. By comparison, off-target binding of [^{18}F]MK-6240 in these regions is low. Off-target

binding of [^{18}F]flortaucipir in choroid plexus was frequent but variable, with 9 of 15 subjects showing elevated signal (SUVR > 1.0 in either hemisphere) and extreme values (SUVR > 2) in one subject (NC5) who was amyloid-negative and tau negative in MTL and NEO by visual assessment. The remaining [^{18}F]flortaucipir images and all [^{18}F]MK-6240 images showed low off-target binding in choroid plexus. In striatum, off-target binding of [^{18}F]flortaucipir was approximately 56% higher than [^{18}F]MK-6240 on average (SUVR of 1.45±0.12 vs 0.93±0.18) and the ranges of striatal SUVR values for the two tracers overlapped in only 3/15 subjects (Figure 4). 6 of 15 subjects showed increased [^{18}F]MK-6240 signal (SUVR > 1.0) at the pial surface of the brain centered on the meninges (Figure 4), although meningeal SUVR outcomes were highly correlated (r^2 = 0.68; $p < 0.001$) between tracers.

In another group of six subjects, all female, we noted conspicuous signal from both radiotracers arising from an overgrowth of bony tissue on the internal surface of the calvarium, consistent with hyperostosis frontalis interna (*30*), which was apparent on computed tomography and MR images (Figure 5). Hyperostosis is a common benign radiographic finding in post-menopausal females (*31*) and is considered to be an x-chromosome linked abnormality (*32*). In some subjects, CT scans revealed other sites of calcification or ossification corresponding to areas of increased [^{18}F]MK-6240 and [^{18}F]flortaucipir off-target signal, which included the pineal gland, the meninges of the falx cerebri, and other focal meningeal calcifications. These features were sometimes noted in the absence of more generalized meningeal [^{18}F]MK-6240 off-target binding, as in NC1 and NC4 (Figure 5).

Voxel-Based Analyses

T-value maps comparing patterns of [^{18}F]flortaucipir and [^{18}F]MK-6240 retention are shown in Figure 6 and reflect off-target binding patterns. Clusters of voxels in which [^{18}F]flortaucipir retention is significantly greater than [^{18}F]MK-6240 were evident in striatum, brainstem, and subcortical and cerebellar white matter (Figure 6, row A). The voxels in which [^{18}F]MK-6240

retention is significantly greater than [^{18}F]flortaucipir were limited to the meninges and bone (Figure 6, row B). Clusters of significant voxels in cortical gray matter where tau pathology is concentrated were not observed in either direction.

DISCUSSION

Amyloid radiotracers in human subjects with typical AD-dementia show a consistent pattern of pathology across tracers and subjects despite differences in dynamic signal range and non-specific binding characteristics (*33-36*). The similarity in the brain distribution of specific signal between Aβ radiotracers has facilitated standardization techniques, such as Centiloid scaling (*37,38*), and is likely attributable to a single human isoform of fibrillar Aβ constituting a distinct brain pathology, amyloid plaques, that is the dominant signal source for Aβ in vivo imaging agents (*39,40*). Tau is considerably more complex with six human isoforms, more post-translational modifications, a greater diversity of pathologic lesions (i.e., NFT, astroglial and oligodendroglial tau inclusions, Pick bodies, etc.), stages of tangle maturity (*41*) and ultrastructural conformations (i.e., PHF, straight filaments, twisted filaments), although in AD the most prevalent species are NFT comprising a PHF combination of 3R and 4R tau isoforms (*42,43*). In vitro binding studies of flortaucipir and MK-6240 suggest low affinity to tau pathologies other than PHF-tau (*17,29,44-46*), although a few in vivo imaging studies have suggested possible/weak sensitivity of [^{18}F]flortaucipir to 4R-tau deposits in some primary tauopathies (*47-49*).

As suggested by autoradiography (*44*), the present study suggests [^{18}F]flortaucipir and [^{18}F]MK-6240 are almost certainly detecting the same AD- and age-related tau pathology. This is evidenced by the similarity of radiotracer retention patterns across a spectrum of disease (Figure 2), highly correlated SUVR outcomes across Braak stage regions, and voxel-based analyses that show no differences in patterns of specific binding to pathologic tau deposits

(Figure 6). In some Braak regions, we observed a slightly elevated floor signal for [^{18}F]flortaucipir compared to [^{18}F]MK-6240, suggesting the former to have slightly higher non-specific retention. This was most apparent in Braak II, which is likely attributable to spill-in from off-target binding of [^{18}F]flortaucipir in choroid plexus.

Our approach to visual interpretation of [^{18}F]flortaucipir and [^{18}F]MK-6240 images was intended to mirror a clinical nuclear medicine environment, albeit with slightly more granularity than a global rating. Although we observed only one instance in our small cohort where a subject (MCI1) was adjudicated overall to be either positive in MTL or NEO, but not both, conceivably distinct ratings for MTL and NEO tau signal may provide some differentiation of the diverse tau phenotypes previously described (*3*) and also, considering Aβ status, help to differentiate AD pathology from normal aging processes (e.g. primary age-related tauopathy (PART)) characterized by MTL tau deposits that may occur independently of Aβ (*50,51*).

Although we observed differences between tracers in dynamic signal range and off-target binding, we expected either would perform well in visual assessments, where off-target binding can be more easily accounted for. This is supported by our results, which showed complete concordance between tracers in overall ratings for both MTL and NEO (Table 2) and substantial agreement between raters ($\kappa > 0.73$, Table 3), regardless of tracer or region.

Comparing visual assessments with diagnoses, both MTL and NEO tau pathology was present in all AD subjects. Among NC subjects 7/9 showed no evidence of tau pathology in either MTL or NEO, whereas NC1 and NC4 were positive in both and had the highest PiB SUVR values of all NC subjects, although only NC1 was quantitatively Aβ-positive (PiB CL = 50). The MCI subject, who was Aβ-negative (PiB CL= 0), was tau-positive only in MTL. This subject may be an example of PART.

Comparison of SUVR images shows that both [^{18}F]flortaucipir and [^{18}F]MK-6240 indicate the same tau pathology, although [^{18}F]MK-6240 shows a nearly two-fold higher dynamic range

(Figure 3) as indexed by regression slopes ranging from 1.45 to 1.98. Similar cerebellar grey matter SUV values between [^{18}F]flortaucipir and [^{18}F]MK-6240, which are used to compute SUVR, indicates that this observation is not attributable to differences in non-specific retention. In vitro saturation binding studies of [^{3}H]MK-6240 and [^{3}H]flortaucipir conducted using the same AD tissue homogenates shows [^{3}H]MK-6240 to have a 3- to 10-fold higher affinity (K_D) for PHF-tau than [^{3}H]flortaucipir, and a 3-5 fold higher B_{max}/K_D ratio (*17,46*). Indeed, differences in the pharmacologic properties may reasonably explain the increased dynamic range of [^{18}F]MK-6240 SUVR, although other factors such as non-specific binding, radiotracer metabolism, and rates of plasma and reference region clearance may influence in vivo specific binding measures. Although both tracers appeared to be well suited to visual interpretation, the greater dynamic range of [^{18}F]MK-6240 may represent an advantage for longitudinal studies of tau progression or treatment response, where detecting small interval changes is key.

An examination of the dispersion of the SUVR data (Figure 3) shows that for all regions except Braak II there is a subject cluster with SUVR values ~ 1 for both radiotracers that includes all subjects visually adjudicated to be negative, whereas the positive cases cover a much broader range with few subjects overlapping with the negative cluster. These few visually positive subjects with low SUVR values likely represent subjects for whom the raters identified focally intense radiotracer uptake, but that the focus of increased signal was diluted in the averaging of all of the voxels in the respective Braak stage region- such as the relatively large Braak III-VI regions shown in Figure 1. An example of such a case is AD1 (Figure 2), which shows a clear unilateral focus of increased uptake in the left precuneus that by visual ratings was indicated as positive for MTL and NEO with both radiotracers, but [^{18}F]flortaucipir and [^{18}F]MK-6240 SUVR values for the Braak V region in this subject were only 1.16 and 1.09. This highlights a potential limitation of sampling PET images of tau radiotracers in accordance with Braak staging. Another complication is that in some elderly subjects with or without cognitive impairment, significant medial temporal lobe (Braak stage I-III region) pathology may

occur independently of Aβ. These cases may represent instances of PART. Therefore, classifying tau status (T+/T-) based on MTL pathology alone would presumably reduce the specificity of a pathologic diagnosis of AD. It is likely that the most sensitive and specific indicators of tau lesions consistent with AD neuropathologic change will require tau PET positivity beyond MTL structures. However, the Braak IV region is relatively large and potentially suffers from the limitation of diluting focal signal that might be the earliest indicator of neocortical spread of tau pathology. For this reason, others have moved towards a data-driven approach with a more granular tissue sampling strategy (*52*).

[^{18}F]flortaucipir images often exhibit elevated off-target binding in striatum and choroid plexus (Figure 4), as well as other tissues, which may occur independently of neurodegenerative disease pathology as previously reported (*6*). For [^{18}F]MK-6240, the frequent observation of elevated signal arising from the meninges and other extracerebral structures (Figure 4) was in accordance with previous observations (*21*). In some cases, it was apparent that spill-in of off-target [^{18}F]MK-6240 signal from the meninges could impact the quantification of signal in cortical brain regions as well as cerebellum, although the fact that meningeal off-target signal is not apparent on [^{18}F]flortaucipir images, yet the SUVR outcomes of [^{18}F]flortaucipir and [^{18}F]MK-6240 are highly correlated (Figure 3), suggests that this does not represent a major confound.

The off-target signal in bone observed with both tracers, most notably in female subjects with HFI, does not appear to be completely explained by in vivo defluorination of these tracers as we did not observe widespread bone uptake consistent with [^{18}F]fluoride scans and the inspection of batch records from our [^{18}F]MK-6240 radiosyntheses did not show evidence of significant residual [^{18}F]fluoride in the injectate. Intracranial calcifications are a common and normal age-related radiographic finding, often described in the pineal gland, the habenula, the choroid plexus, basal ganglia, falx cerebri, dura mater, petroclinoid ligaments, superior sagittal sinus, as well as the dentate nuclei of the cerebellum and the hippocampus (*53*). Interestingly,

these regions overlap with areas where off-target binding of these tau radiotracers is often observed, but inspection of low-dose CT scans showed no macroscopic calcifications in the choroid plexus of our study subjects.

Limitations of the present study include a small sample size and a limited range of pathology and degree of clinical impairment. Only one of nine NC subjects was globally A+ and the only MCI subject was A- . The five AD subjects studied showed mild to moderate cognitive impairment and we observed relatively limited tau pathology in Braak stages V and VI across the sample. Given the small sample size of our pathologically heterogeneous cohort, in which cases with advanced tau pathology comprise over one third of the study cohort, our measures of interrater reliability may not be able to be generalized to other subject cohorts. We would expect there to be considerably less agreement and lower reliability in studies of cohorts that were comprised predominantly of cognitively normal elderly where tau burden is less. Indeed, we observed some discordance between raters among non-demented subjects (Supplementary Figure 4). In our study, [^{18}F]MK-6240 injected doses were limited to 185 MBq to meet the University of Pittsburgh's RDRC organ dosimetry limits. Another limitation of the present study was the lack of measures of intra-rater reliability, as the small size and high disease burden in our cohort would be expected to yield a high level of intra-rater reliability that also could not be generalized to other cohorts.

CONCLUSION

The direct comparison of brain distribution, specific signal, and off-target binding of [^{18}F]flortaucipir and [^{18}F]MK-6240 in the same subjects suggests that these tau radiotracers indicate the same tau pathology and reflect Braak stages of NFT pathology. The off-target binding pattern was frequently observed in choroid plexus and striatum for [^{18}F]flortaucipir and in meninges for [^{18}F]MK-6240. Complete concordance in visual ratings of tau positivity suggests that both radiotracers can be expected to perform well for visual interpretation of images,

although studies in larger cohorts across the entire spectrum of tau accumulation are needed to test the limits of visual rating methods. Differential ratings for MTL and NEO may be useful for discriminating tau AD phenotypes and also for differentiating AD neuropathologic changes from age-related tau deposition, although this methodology will also require further study. We observed [^{18}F]MK-6240 to have an approximately two-fold greater dynamic range in specific signal across the range of pathology present in our subject cohort, possibly due to its higher affinity to PHF-tau. This may be an important consideration for planning longitudinal studies where the detection of small changes in tau load indices over relatively short periods is of paramount importance.

ACKNOWLEDGEMENTS

This work was supported by grants from the National Institute of Aging, AG025204 and AG005133. We thank the staff of the University of Pittsburgh PET Facility and the Alzheimer's Disease Research Center for their assistance.

KEY POINTS

QUESTION: What are the cross-sectional differences in on- and off-target binding of the two most commonly used tau-PET imaging agents?

PERTINENT FINDINGS: The head-to-head comparison of [^{18}F]flortaucipir and [^{18}F]MK-6240 showed very similar relative levels of radiotracer retention in most cortical regions in both tau-negative and tau-positive cases, suggesting that these agents have very similar on-target binding to PHF tau- the prevalent form in AD. However, there were important differences in off-target binding characteristics in choroid plexus, striatum and meninges.

IMPLICATIONS FOR PATIENT CARE: These tau-PET imaging agents provide similar estimation of the presence of PHF tau related to AD, but care must be taken to understand the influence of off-target binding in the interpretation of each specific tracer.

REFERENCES

1. Hardy JA, Higgins GA. Alzheimer's disease: The amyloid cascade hypothesis. *Science.* 1992;256:184-185.

2. Scholl M, Lockhart SN, Schonhaut DR, et al. PET imaging of tau deposition in the aging human brain. *Neuron.* 2016;89:971-982.

3. Ossenkoppele R, Schonhaut DR, Scholl M, et al. Tau PET patterns mirror clinical and neuroanatomical variability in Alzheimer's disease. *Brain.* 2016;139:1551-1567.

4. Leuzy A, Chiotis K, Lemoine L, et al. Tau PET imaging in neurodegenerative tauopathies-still a challenge. *Mol Psychiatry.* 2019;24:1112-1134.

5. Saint-Aubert L, Lemoine L, Chiotis K, Leuzy A, Rodriguez-Vieitez E, Nordberg A. Tau PET imaging: Present and future directions. *Mol Neurodegener.* 2017;12:19. doi: 10.1186/s13024-017-0162-3

6. Johnson KA, Schultz A, Betensky RA, et al. Tau positron emission tomographic imaging in aging and early Alzheimer disease. *Ann Neurol.* 2016;79:110-119.

7. Villemagne VL, Doré V, Bourgeat P, et al. Aβ-amyloid and tau imaging in dementia. *Seminars in Nuclear Medicine.* 2017;47:75-88.

8. Chien DT, Bahri S, Szardenings AK, et al. Early clinical PET imaging results with the novel PHF-tau radioligand ^{18}F-T807. *J Alzheimers Dis.* 2013;34:457-468.

9. Walji AM, Hostetler ED, Selnick H, et al. Discovery of 6-(Fluoro-^{18}F)-3-(1H-pyrrolo[2,3-C]pyridin-1-yl)isoquinolin-5-amine (^{18}F-MK-6240): A positron emission tomography (PET) imaging agent for quantification of neurofibrillary tangles (NFTs). *J Med Chem.* 2016;59:4778-4789.

10. Fleisher AS, Pontecorvo MJ, Devous MD, Sr., et al. Positron emission tomography imaging with ^{18}F-flortaucipir and postmortem assessment of Alzheimer disease neuropathologic changes. *JAMA Neurol.* 2020;77:829-839.

11. Braak H, Braak E. Staging of Alzheimer's disease-related neurofibrillary changes. *Neurobiol Aging.* 1995;16:271-278; discussion 278-284.

12. Ossenkoppele R, Rabinovici GD, Smith R, et al. Discriminative accuracy of ^{18}F-flortaucipir positron emission tomography for Alzheimer disease vs other neurodegenerative disorders. *JAMA.* 2018;320:1151-1162.

13. Shcherbinin S, Schwarz AJ, Joshi A, et al. Kinetics of the tau PET tracer ^{18}F-AV-1451 (T807) in subjects with normal cognitive function, mild cognitive impairment, and Alzheimer disease. *J Nucl Med.* 2016;57:1535-1542.

14. Devous MD, Sr., Joshi AD, Navitsky M, et al. Test-retest reproducibility for the tau PET imaging agent flortaucipir F 18. *J Nucl Med.* 2018;59:937-943.

15. Zhao Q, Liu M, Ha L, Zhou Y, Alzheimer's Disease Neuroimaging I. Quantitative ^{18}F-AV1451 brain tau PET imaging in cognitively normal older adults, mild cognitive impairment, and Alzheimer's disease patients. *Front Neurol.* 2019;10:486. doi:10.3389/fneur.2019.00486

16. Baker SL, Harrison TM, Maass A, La Joie R, Jagust WJ. Effect of off-target binding on ^{18}F-flortaucipir variability in healthy controls across the life span. *J Nucl Med.* 2019;60:1444-1451.

17. Hostetler ED, Walji AM, Zeng Z, et al. Preclinical characterization of ^{18}F-MK-6240, a promising PET tracer for in vivo quantification of human neurofibrillary tangles. *J Nucl Med.* 2016;57:1599-1606.

18. Lohith TG, Bennacef I, Vandenberghe R, et al. Brain imaging of Alzheimer dementia patients and elderly controls with ^{18}F-MK-6240, a PET tracer targeting neurofibrillary tangles. *J Nucl Med.* 2019;60:107-114.

19. Pascoal TA, Shin M, Kang MS, et al. In vivo quantification of neurofibrillary tangles with ^{18}F-MK-6240. *Alzheimers Res Ther.* 2018;10:74. doi:10.1186/s13195-018-0402-y

20. Guehl NJ, Wooten DW, Yokell DL, et al. Evaluation of pharmacokinetic modeling strategies for in-vivo quantification of tau with the radiotracer ^{18}F-MK-6240 in human subjects. *Eur J Nucl Med Mol Imaging.* 2019;46:2099-2111.

21. Betthauser TJ, Cody KA, Zammit MD, et al. In vivo characterization and quantification of neurofibrillary tau PET radioligand ^{18}F-MK-6240 in humans from Alzheimer disease dementia to young controls. *J Nucl Med.* 2019;60:93-99.

22. Salinas C, Lohith TG, Purohit A, et al. Test-retest characteristic of ^{18}F-MK-6240 quantitative outcomes in cognitively normal adults and subjects with Alzheimer's disease. *J Cereb Blood Flow Metab.* 2020;40(11):2179-2087.

23. Pascoal TA, Therriault J, Benedet AL, et al. ^{18}F-MK-6240 PET for early and late detection of neurofibrillary tangles. *Brain.* 2020;143:2818-2830.

24. Jack CR, Jr., Albert MS, Knopman DS, et al. Introduction to the recommendations from the National Institute on Aging-Alzheimer's Association workgroups on diagnostic guidelines for Alzheimer's disease. *Alzheimers Dement.* 2011;7:257-262.

25. Okonkwo DO, Puffer RC, Minhas DS, et al. ^{18}F-FDG, ^{11}C-PIB, and ^{18}F-AV-1451 PET imaging of neurodegeneration in two subjects with a history of repetitive trauma and cognitive decline. *Front Neurol.* 2019;10:831. doi:10.3389/fneur.2019.00831

26. McNamee RL, Yee SH, Price JC, et al. Consideration of optimal time window for Pittsburgh compound-B PET summed uptake measurements. *J Nucl Med.* 2009;50:348-355.

27. Fischl B, van der Kouwe A, Destrieux C, et al. Automatically parcellating the human cerebral cortex. *Cereb Cortex.* 2004;14:11-22.

28. Baker SL, Lockhart SN, Price JC, et al. Reference tissue-based kinetic evaluation of ^{18}F-AV-1451 for tau imaging. *J Nucl Med.* 2017;58:332-338.

29. Marquie M, Normandin MD, Vanderburg CR, et al. Validating novel tau positron emission tomography tracer ^{18}F-AV-1451 (T807) on postmortem brain tissue. *Ann Neurol.* 2015;78:787-800.

30. She R, Szakacs J. Hyperostosis frontalis interna: Case report and review of literature. *Annals of Clinical & Laboratory Science.* 2004;34:206-208.

31. May H, Peled N, Dar G, Abbas J, Hershkovitz I. Hyperostosis frontalis interna: What does it tell us about our health? *Am J Hum Biol.* 2011;23:392-397.

32. Hershkovitz I, Greenwald C, Rothschild BM, et al. Hyperostosis frontalis interna: An anthropological perspective. *American Journal of Physical Anthropology.* 1999;109:303-325.

33. Landau SM, Thomas BA, Thurfjell L, et al. Amyloid PET imaging in Alzheimer's disease: A comparison of three radiotracers. *Eur J Nucl Med Mol Imaging.* 2014;41:1398-1407.

34. Wolk DA, Zhang Z, Boudhar S, Clark CM, Pontecorvo MJ, Arnold SE. Amyloid imaging in Alzheimer's disease: Comparison of florbetapir and Pittsburgh compound-B positron emission tomography. *J Neurol Neurosurg Psychiatry.* 2012;83:923-926.

35. Morbelli S, Bauckneht M. Amyloid PET imaging: Standardization and integration with other Alzheimer's disease biomarkers. *Methods Mol Biol.* 2018;1750:203-212.

36. Villemagne VL, Mulligan RS, Pejoska S, et al. Comparison of ^{11}C-PIB and ^{18}F-florbetaben for Abeta imaging in ageing and Alzheimer's disease. *Eur J Nucl Med Mol Imaging.* 2012;39:983-989.

37. Whittington A, Gunn RN, Alzheimer's Disease Neuroimaging I. Amyloid load: A more sensitive biomarker for amyloid imaging. *J Nucl Med.* 2019;60:536-540.

38. Klunk WE, Koeppe RA, Price JC, et al. The centiloid project: Standardizing quantitative amyloid plaque estimation by PET. *Alzheimers Dement.* 2015;11:1-15 e11-14.

39. Klunk WE, Lopresti BJ, Ikonomovic MD, et al. Binding of the positron emission tomography tracer Pittsburgh compound-B reflects the amount of amyloid-beta in Alzheimer's disease brain but not in transgenic mouse brain. *J Neurosci.* 2005;25:10598-10606.

40. Klunk WE, Wang Y, Huang GF, et al. The binding of 2-(4'-methylaminophenyl)benzothiazole to postmortem brain homogenates is dominated by the amyloid component. *J Neurosci.* 2003;23:2086-2092.

41. Lowe VJ, Curran G, Fang P, et al. An autoradiographic evaluation of AV-1451 tau PET in dementia. *Acta Neuropathol Commun.* 2016;4:58. doi:10.1186/s40478-016-0315-6

42. Iqbal K, Alonso Adel C, Chen S, et al. Tau pathology in Alzheimer disease and other tauopathies. *Biochim Biophys Acta.* 2005;1739:198-210.

43. Naseri NN, Wang H, Guo J, Sharma M, Luo W. The complexity of tau in Alzheimer's disease. *Neurosci Lett.* 2019;705:183-194.

44. Aguero C, Dhaynaut M, Normandin MD, et al. Autoradiography validation of novel tau pet tracer ^{18}F-MK-6240 on human postmortem brain tissue. *Acta Neuropathol Commun.* 2019;7:37. doi:10.1186/s40478-019-0686-6

45. Marquie M, Normandin MD, Meltzer AC, et al. Pathological correlations of ^{18}F-AV-1451 imaging in non-Alzheimer tauopathies. *Ann Neurol.* 2017;81:117-128.

46. Lindberg A, Knight AC, Sohn D, et al. Radiosynthesis, in vitro and in vivo evaluation of ^{18}F-CBD-2115 as a first-in-class radiotracer for imaging 4R-tauopathies. *ACS Chem Neurosci.* 2021;12:596-602.

47. Passamonti L, Vazquez Rodriguez P, Hong YT, et al. ^{18}F-AV-1451 positron emission tomography in Alzheimer's disease and progressive supranuclear palsy. *Brain.* 2017;140:781-791.

48. Whitwell JL, Ahlskog JE, Tosakulwong N, et al. Pittsburgh compound B and AV-1451 positron emission tomography assessment of molecular pathologies of Alzheimer's disease in progressive supranuclear palsy. *Parkinsonism Relat Disord.* 2018;48:3-9.

49. Smith R, Schain M, Nilsson C, et al. Increased basal ganglia binding of ^{18}F-AV-1451 in patients with progressive supranuclear palsy. *Mov Disord.* 2017;32:108-114.

50. Josephs KA, Murray ME, Tosakulwong N, et al. Tau aggregation influences cognition and hippocampal atrophy in the absence of beta-amyloid: A clinico-imaging-pathological study of primary age-related tauopathy (PART). *Acta Neuropathol.* 2017;133:705-715.

51. Crary JF, Trojanowski JQ, Schneider JA, et al. Primary age-related tauopathy (PART): A common pathology associated with human aging. *Acta Neuropathol.* 2014;128:755-766.

52. Jack CR, Jr., Wiste HJ, Schwarz CG, et al. Longitudinal tau PET in ageing and Alzheimer's disease. *Brain.* 2018;141:1517-1528.

53. Saade C, Najem E, Asmar K, Salman R, El Achkar B, Naffaa L. Intracranial calcifications on CT: An updated review. *J Radiol Case Rep.* 2019;13:1-18.

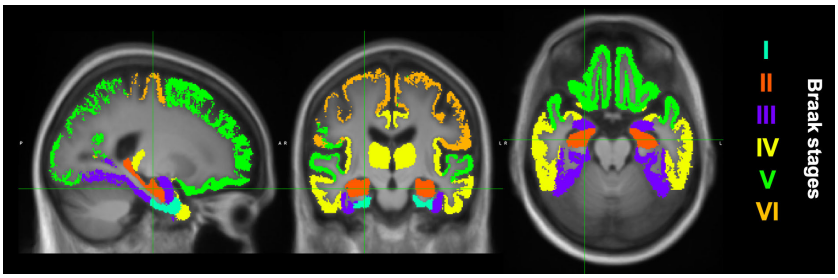

Figure 1: Grouping of FreeSurfer regions to correspond with Braak pathological stages (I-VI).

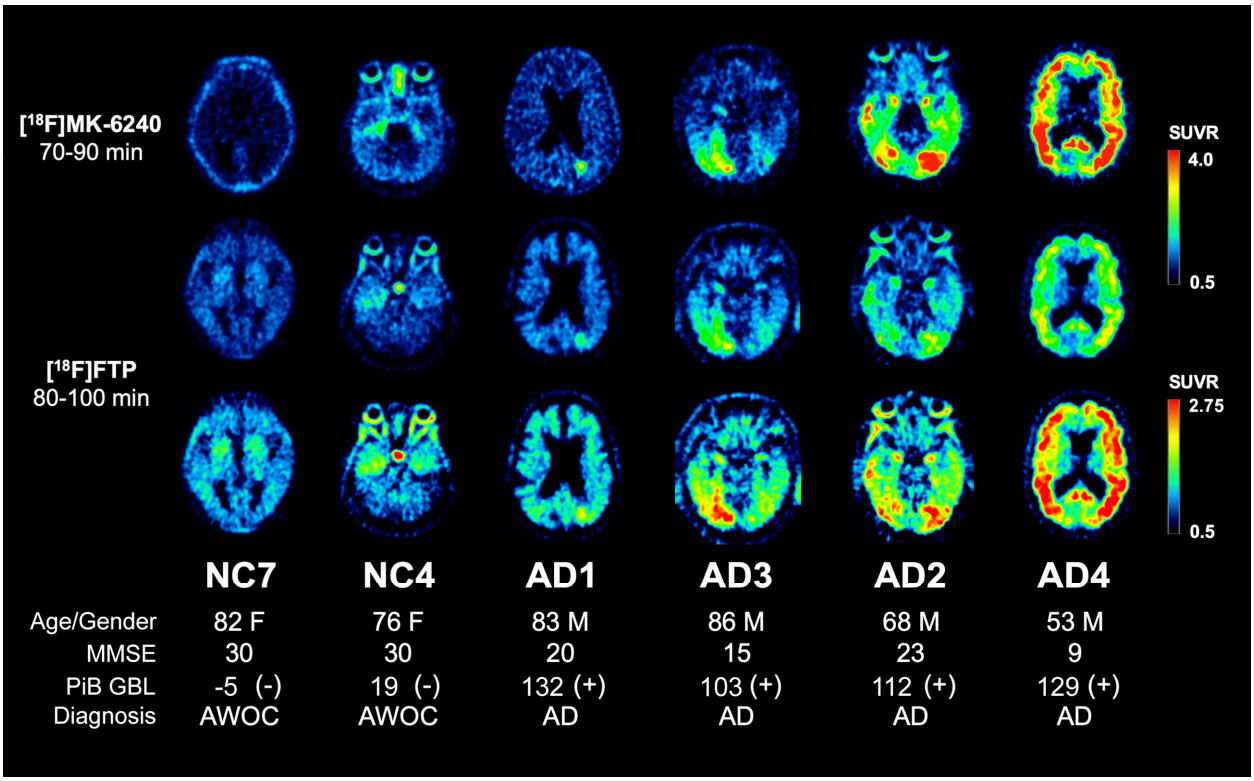

Figure 2: [18F]flortaucipir ([18F]FTP) and [18F]MK-6240 SUVR images from six subjects representing the range of tau pathology observed in our cohort. From left to right : a subject showing no evidence of tau pathology (NC7); a cognitively normal subject showing early Braak stage pathology (NC4); an atypical AD subject with tau pathology in the MTL and evidence of focal uptake in Braak V (AD1); three AD subjects showing a progression of increasingly severe tau pathology culminating with widespread neocortical involvement in AD4. [18F]FTP and [18F]MK-6240 are shown on a common scale (SUVR: 0.5 - 4.0). [18F]FTP images are repeated (row 3) on a compressed scale (SUVR: 0.5 - 2.75) so that subtle differences may be more appreciated. The data point representing AD1 is shown to illustrate the dilution of visually evident focal tau signal in the large Braak-stage regions.

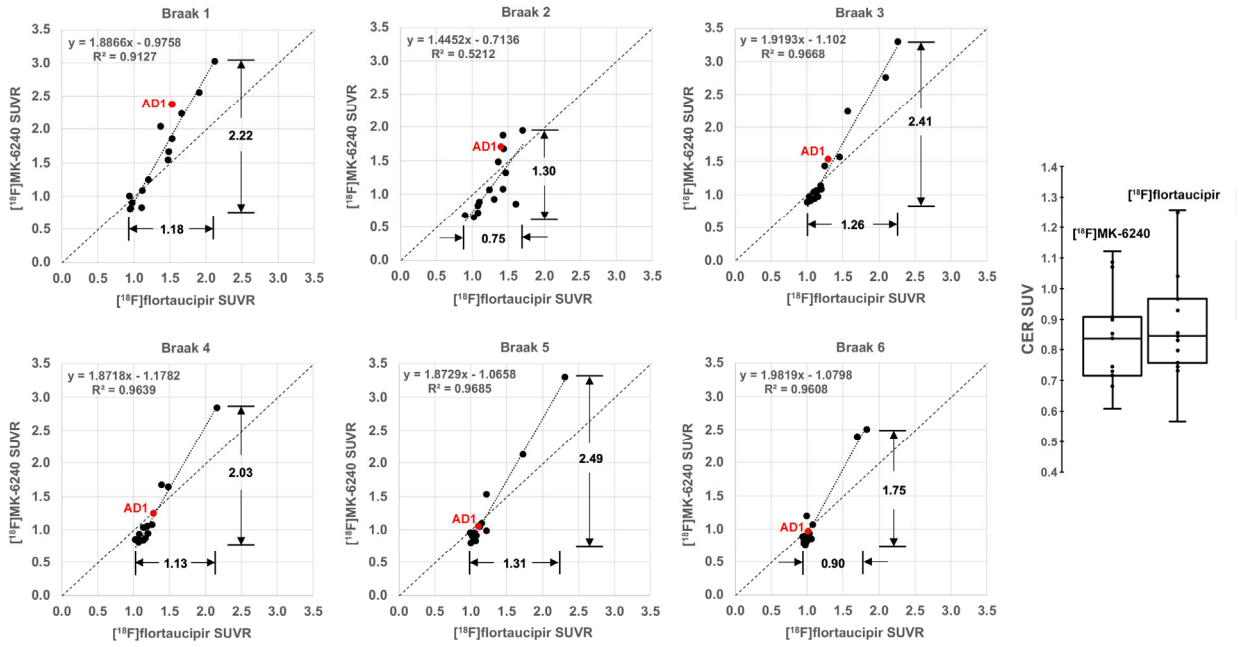

Figure 3: Comparison of [^{18}F]flortaucipir ([^{18}F]FTP) and [^{18}F]MK-6240 SUVR outcomes across six Braak stage regions, showing a linear regression of values. For each Braak stage region, the dynamic range of SUVR outcomes is indicated.

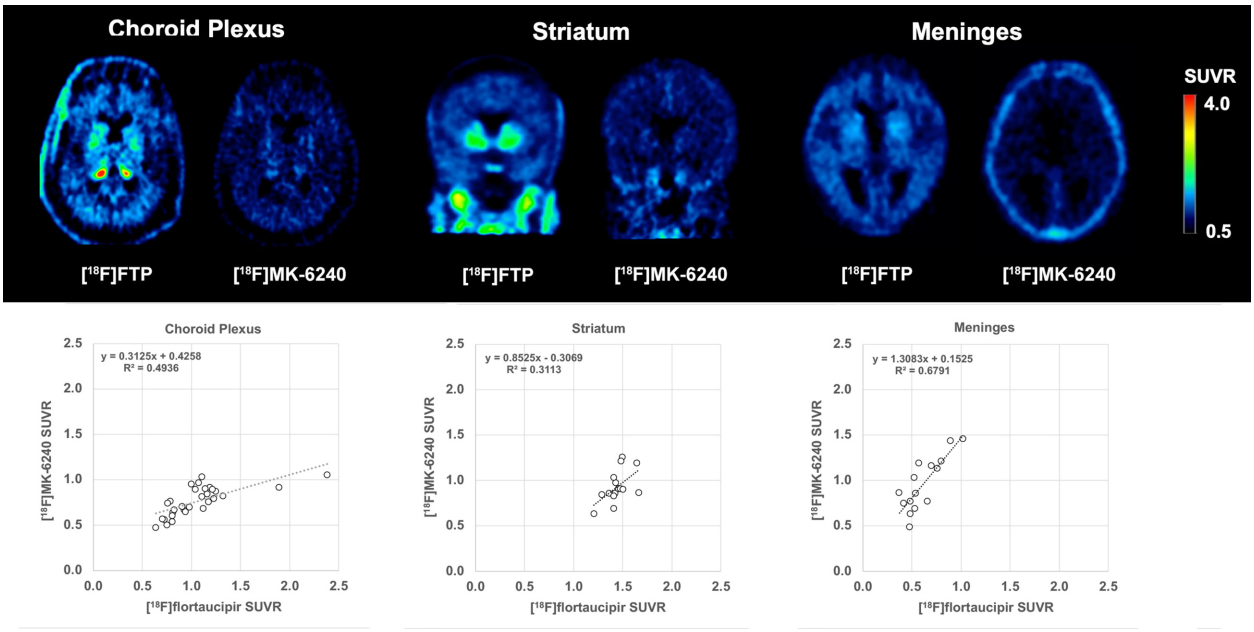

Figure 4: A comparison of off-target binding of [^{18}F]flortaucipir ([^{18}F]FTP) and [^{18}F]MK-6240 in choroid plexus, striatum, and meninges. Shown are representative images of typical patterns of off-target retention in these regions (top). The distribution of SUVR outcomes are also shown (below).

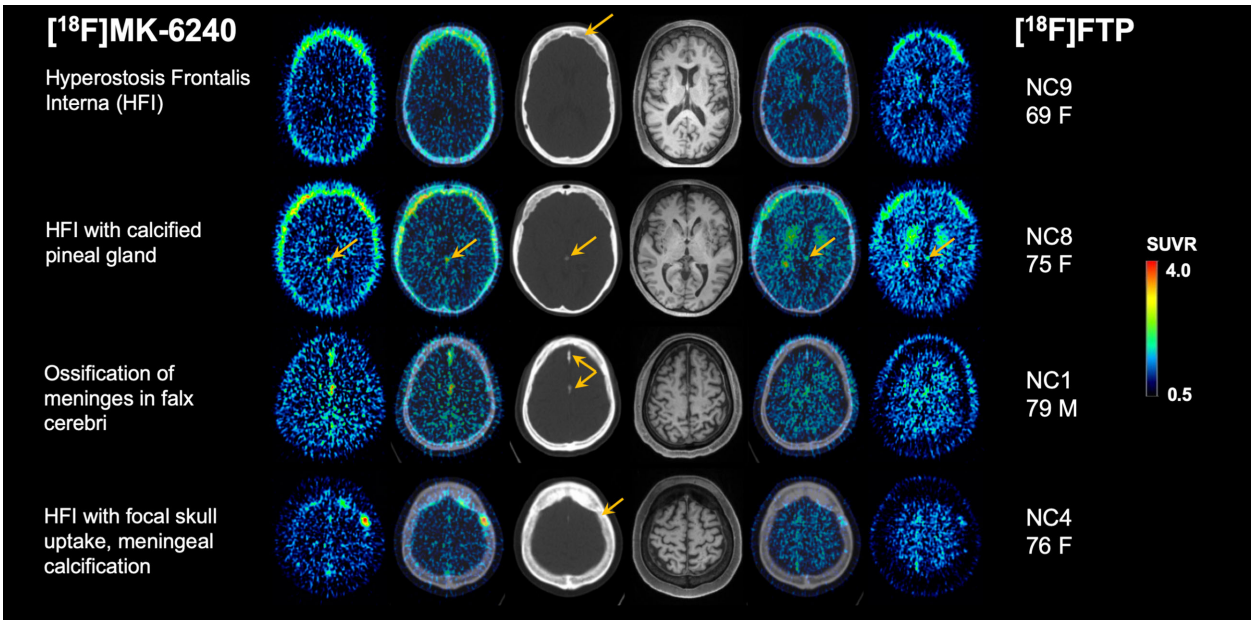

Figure 5: [^{18}F]flortaucipir ([^{18}F]FTP), [^{18}F]MK-6240, CT and MR images of subjects with: (top row) a case of hyperostosis frontalis interna (HFI); (second row) a subject with HFI and a highly calcified pineal gland; (third row) a subject with marked meningeal ossification and calcification in the falx cerebri; and (bottom row) a subject with HFI and a bony lesion of the skull with several small meningeal calcifications.

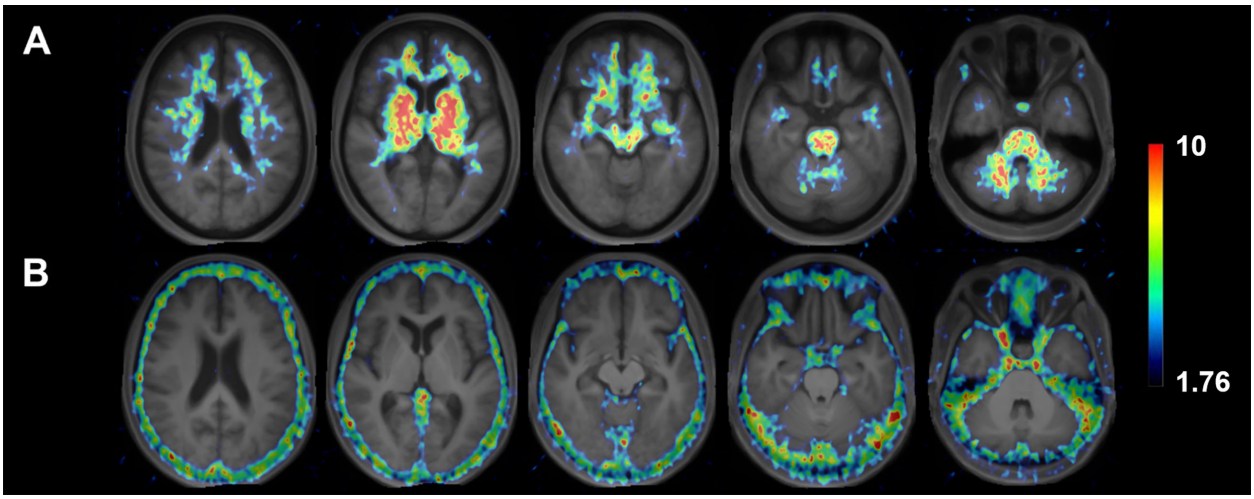

Figure 6: Voxel-based comparison of [^{18}F]flortaucipir ([^{18}F]FTP) and [^{18}F]MK-6240 retention. Shown are T-maps of contrasts where [^{18}F]FTP > [^{18}F]MK-6240 (row A) and also [^{18}F]MK-6240 > [^{18}F]FTP (row B) are significantly different at $p < 0.05$, uncorrected ($T>1.76$). T-maps are shown overlaid on an average MR image generated from the 15 subjects.

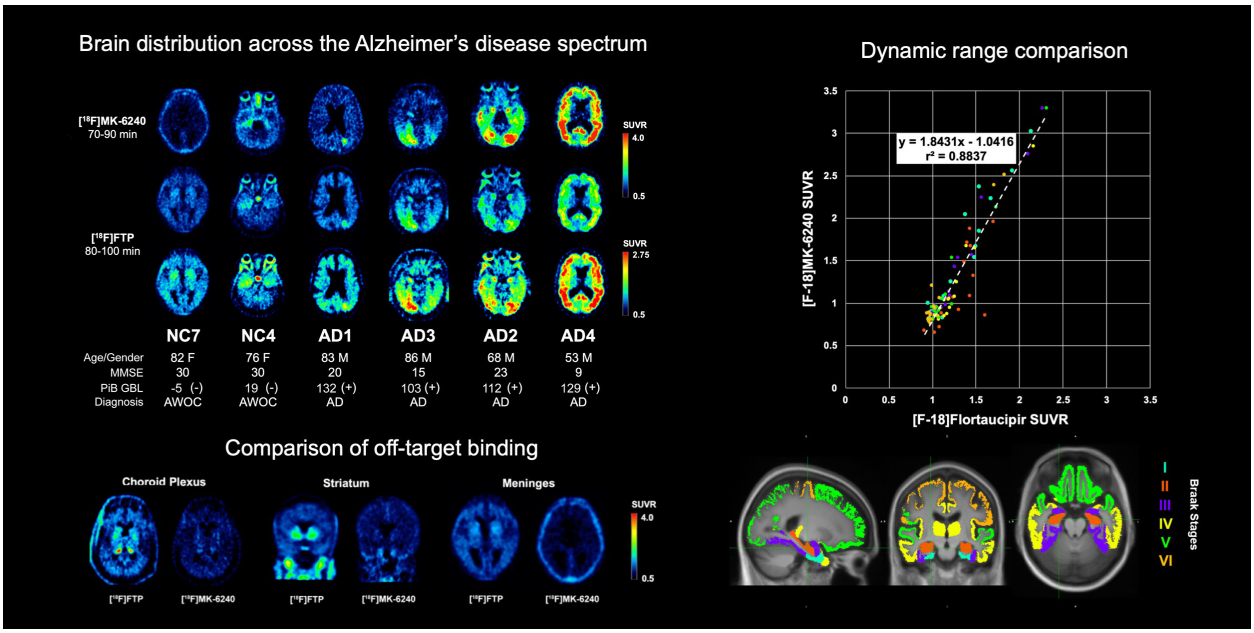

Graphical Abstract

Table 1. Subject characteristics

ID	Age	Gender	Race	MMSE	Education (years)	Scan Interval (days)	Diagnosis
AD1	83	M	C	20	16	2	Probable AD (atypical)
AD2	68	M	C	23	14	6	Probable AD
AD3	86	M	C	15	12	1	Probable AD
AD4	53	M	C	9	12	2	Probable AD
AD5	64	F	C	29	12	1	Probable AD
MCI1	77	M	C	22	12	20	MCI-amnestic + other
NC1	79	F	AA	24	12	7	Abnormal w/o complaint
NC2	79	F	C	30	18	52	Normal cognition
NC3	79	F	AA	28	14	54	Abnormal w/o complaint
NC4	76	F	AA	30	14	48	Abnormal w/o complaint
NC5	76	M	AA	22	11	26	Abnormal w/o complaint
NC6	73	F	C	30	18	24	Abnormal w/o complaint
NC7	82	F	C	30	14	30	Abnormal w/o complaint
NC8	75	F	C	30	14	19	Normal Cognition
NC9	69	F	C	30	16	49	Normal Cognition

Abbreviations used: NC: normal cognition, AD: Alzheimer disease dementia, MCI: mild cognitive impairment, MMSE: mini-mental state examination, C: Caucasian, AA: African-American

Table 2. Visual assessments of [^{18}F]flortaucipir and [^{18}F]MK-6240 scans

Subject	MTL		NEO		PiB GBL		
ID	FTP	MK	FTP	MK	SUVR	Centiloids	Aβ Status
AD1	POS	POS	POS	POS	2.53	132	POS
AD2	POS	POS	POS	POS	2.42	112	POS
AD3	POS	POS	POS	POS	2.3	103	POS
AD4	POS	POS	POS	POS	2.47	129	POS
AD5	POS	POS	POS	POS	2.51	121	POS
MCI1	POS	POS	NEG	NEG	1.24	0	NEG
NC1	POS	POS	POS	POS	1.56	50	POS
NC2	NEG	NEG	NEG	NEG	1.13	-2	NEG
NC3	NEG	NEG	NEG	NEG	1.13	-10	NEG
NC4	POS	POS	POS	POS	1.31	19	NEG
NC5	NEG	NEG	NEG	NEG	1.14	4	NEG
NC6	NEG	NEG	NEG	NEG	1.18	9	NEG
NC7	NEG	NEG	NEG	NEG	1.16	-5	NEG
NC8	NEG	NEG	NEG	NEG	1.21	4	NEG
NC9	NEG	NEG	NEG	NEG	1.29	6	NEG

Table 3. Assessments of interrater reliability of visual ratings

	Tracer	κ* (95% CI)	Z-score	p-value
MTL	FTP	0.836 (0.675 - 0.997)	10.2	<< 0.0001
	MK	0.813 (0.653 - 0.973)	9.96	<< 0.0001
NEO	FTP	0.733 (0.573 - 0.893)	8.98	<< 0.0001
	MK	0.760 (0.600 - 0.920)	9.3	<< 0.0001
All	FTP	0.785 (0.672 - 0.898)	13.6	<< 0.0001
	MK	0.787 (0.674 - 0.900)	13.6	<< 0.0001

*Fleiss' kappa statistic

Visual Assessments

Visual assessments of [^{18}F]flortaucipir and [^{18}F]MK-6240 SUVR parametric images were performed by five experienced raters, all with extensive experience interpreting tau PET images (VLV, JMM, WEK, ADC, TAP). Assessments of all [^{18}F]flortaucipir and [^{18}F]MK-6240 scans were performed using a randomized and anonymized coding scheme that raters were blinded to. All ratings were performed using ITK-SNAP software (v 3.8). PET SUVR images were presented in the same color scale (Jet), and scaled using a fixed lower threshold of SUVR = 0.9 and a sliding upper threshold that was initially set to the maximum image value ($SUVR_{max}$) that could be adjusted by the rater. Raters were presented with the PET images and instructed to provide a rating (positive or negative) for pathologic tau deposits in two areas: the medial temporal lobe (MTL) and neocortex (NEO). The MTL rating considered tau retention in entorhinal cortex, parahippocampus, hippocampus, and amygdala, which are those regions associated with early (Braak I-III) stage pathology. The NEO rating considered tau retention in all cortical regions associated with late Braak stages (IV-VI) and also fusiform and lingual gyri that, despite being associated with Braak III, are considered to be part of the neocortex. Fleiss' kappa (κ) was calculated to assess interrater reliability across tracers and regions. Overall assessments of tau pathology using [^{18}F]flortaucipir and [^{18}F]MK-6240 were determined for MTL and NEO based on a simple majority of the five individual ratings. These overall assessments were used to test for concordance in visual ratings between radiotracers.

Supplementary Table 1. Braak stage corresponding FreeSurfer regions

Braak I	**Braak V**	**Braak V (continued)**
L_entorhinal	L_superior_frontal	R_superior_frontal
R_entorhinal	L_lateral_orbitofrontal	R_lateral_orbitofrontal
	L_medial_orbitofrontal	R_medial_orbitofrontal
Braak II	L_frontal_pole	R_frontal_pole
L_hippocampus	L_caudal_middle_frontal	R_caudal_middle_frontal
R_hippocampus	L_rostral_middle_frontal	R_rostral_middle_frontal
	L_pars_opercularis	R_pars_opercularis
Braak III	L_pars_orbitalis	R_pars_orbitalis
L_parahippocampal	L_pars_triangularis	R_pars_triangularis
L_fusiform	L_caudate*	R_caudate*
L_lingual	L_putamen*	R_putamen*
L_amygdala	L_lateraloccipital	R_lateraloccipital
R_parahippocampal	L_parietalsupramarginal	R_parietalsupramarginal
R_fusiform	L_parietalinferior	R_parietalinferior
R_lingual	L_superiortemporal	R_superiortemporal
R_amygdala	L_pallidum*	R_pallidum*
	L_parietalsuperior	R_parietalsuperior
Braak IV	L_precuneus	R_precuneus
L_middletemporal	L_bankSuperiorTemporalSulcus	R_bankSuperiorTemporalSulcus
L_thalamus	L_accumbens*	R_accumbens*
L_caudantcing	L_tranvtemp	R_tranvtemp
L_rostantcing		
L_postcing		
L_isthmuscing		**VI**
L_insula		L_pericalcarine
L_inferiortemporal		L_postcentral
L_temppole		L_cuneus
R_middletemporal		L_precentral
R_thalamus		L_paracentral
R_caudantcing		R_pericalcarine
R_rostantcing		R_postcentral
R_postcing		R_cuneus
R_isthmuscing		R_precentral
R_insula		R_paracentral
R_inferiortemporal		
R_temppole		

*Excluded from Braak V region because of frequent [^{18}F]flortaucipir off-target binding

Supplementary Figure 1

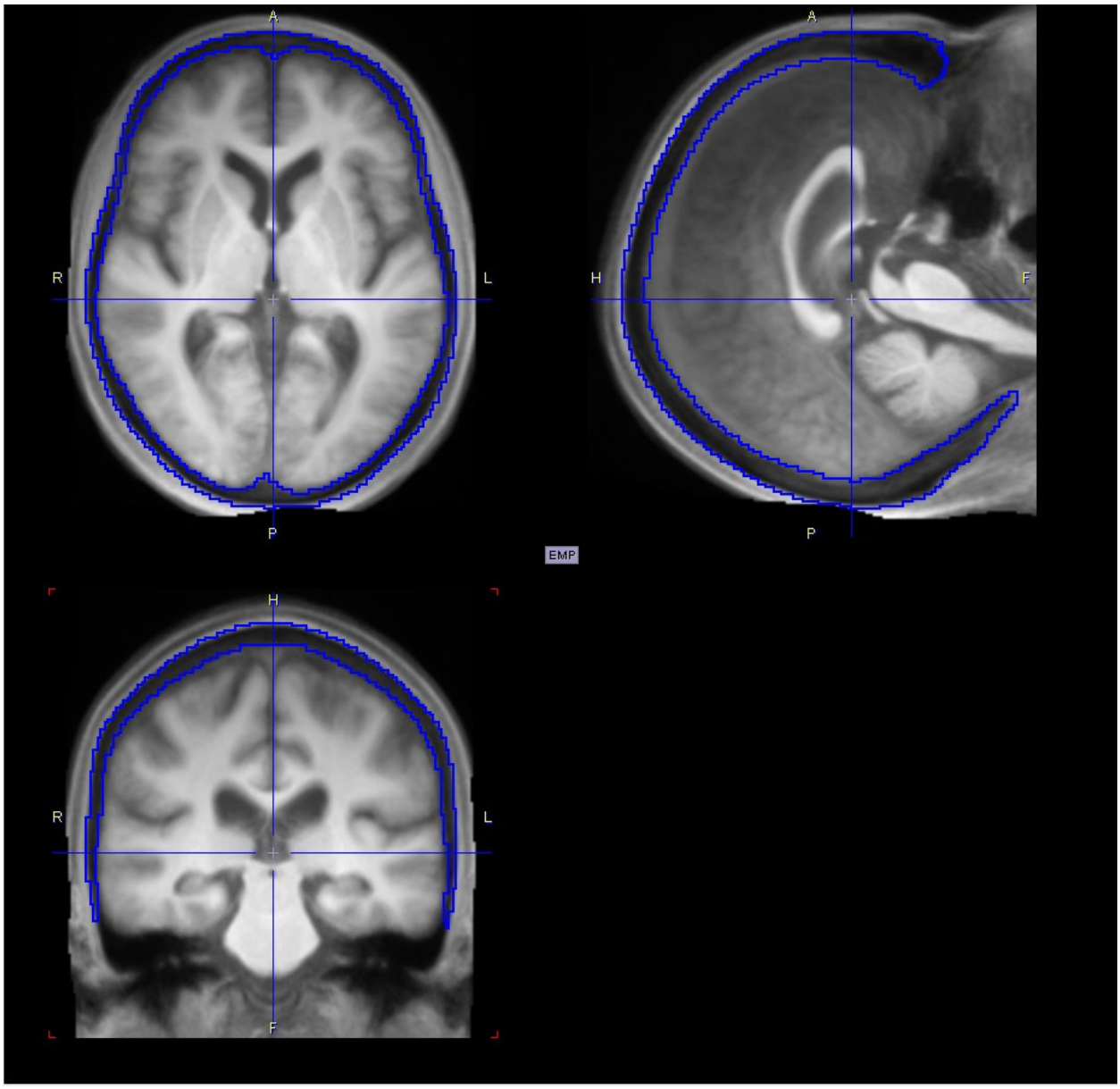

Supplementary Figure 1: Meninges region of interest based on SPM segmentation

Supplementary Figure 2: Comparison of Individual Tau Visual Ratings

Medial Temporal Lobe (MTL) Individual Ratings

Subject	Rater 1		Rater 2		Rater 3		Rater 4		Rater 5		Majority	
ID	FTP	MK	FTP	MK	FTP	MK	FTP	MK	FTP	MK	FTP	MK
AD1											5	5
AD2											5	5
AD3											5	5
AD4											5	5
AD5											5	5
MCI1											5	3
NC1											5	5
NC2											5	4
NC3											5	5
NC4											5	4
NC5											4	5
NC6											4	5
NC7											5	5
NC8											4	5
NC9											5	5

Neocortical (NEO) Individual Ratings)

Subject	Rater 1		Rater 2		Rater 3		Rater 4		Rater 5		Majority	
ID	FTP	MK	FTP	MK	FTP	MK	FTP	MK	FTP	MK	FTP	MK
AD1											5	5
AD2											5	5
AD3											5	5
AD4											5	5
AD5											5	5
MCI1											4	5
NC1											4	5
NC2											5	4
NC3											4	5
NC4											5	3
NC5											5	3
NC6											4	5
NC7											5	5
NC8											5	5
NC9											5	4

Supplementary Figure 2: Individual visual ratings of [^{18}F]flortaucipir and [^{18}F]MK-6240 for pathologic tau deposits in medial temporal lobe (MTL) and neocortex (NEO). Red squares indicate a positive rating whereas green squares indicate negative. A majority rating is also shown along with the number of raters (3 to 5) that comprised the majority.

Supplementary Figure 3

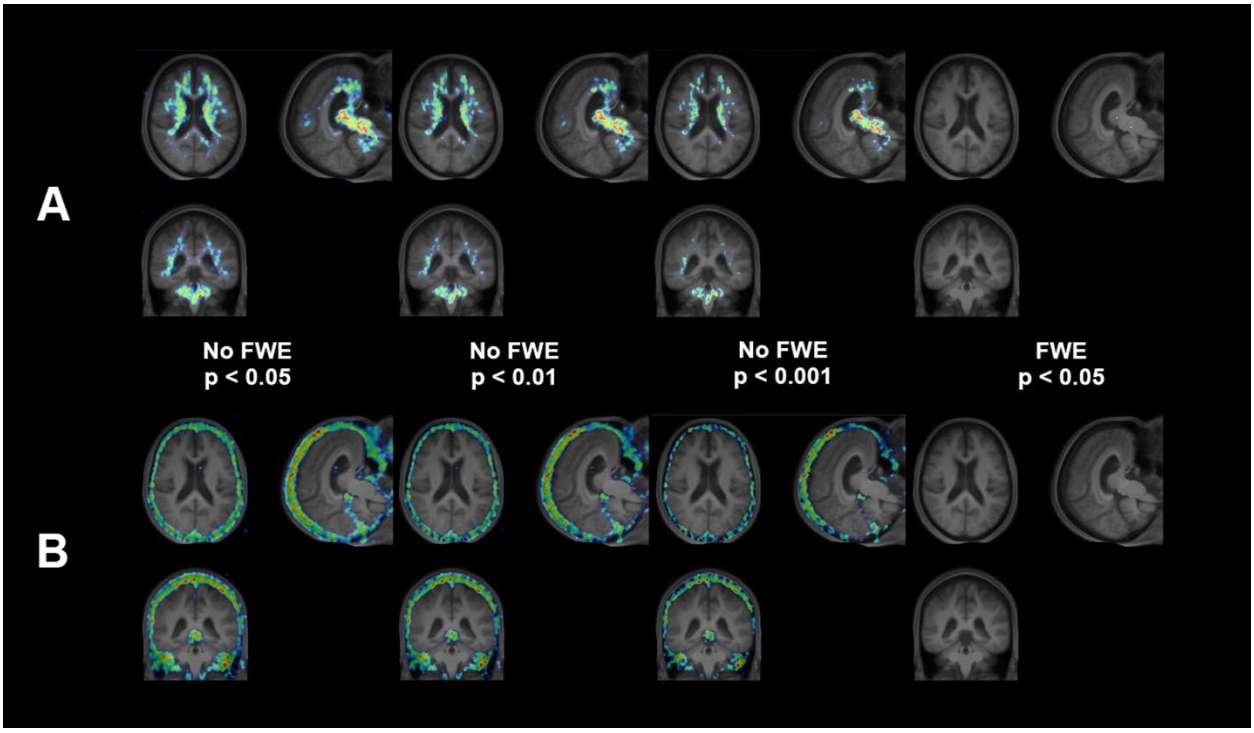

Supplementary Figure 3: Voxel-based comparison of [^{18}F]flortaucipir and [^{18}F]MK-6240 retention. Shown are T-maps of contrasts where [^{18}F]flortaucipir > [^{18}F]MK-6240 (row A) and also [^{18}F]MK-6240 > [^{18}F]flortaucipir (row B) without correction for family-wise error (FWE) at three levels of significance: $p<0.05$, $p<0.01$, and $p<0.001$ and with FWE-correction at $p<0.05$. The T-maps distinctly reflect the differential patterns of off-target retention of the two radiotracers, whereas cortical areas that harbor tau pathology in AD did not show significant differences.

Supplementary Figure 4

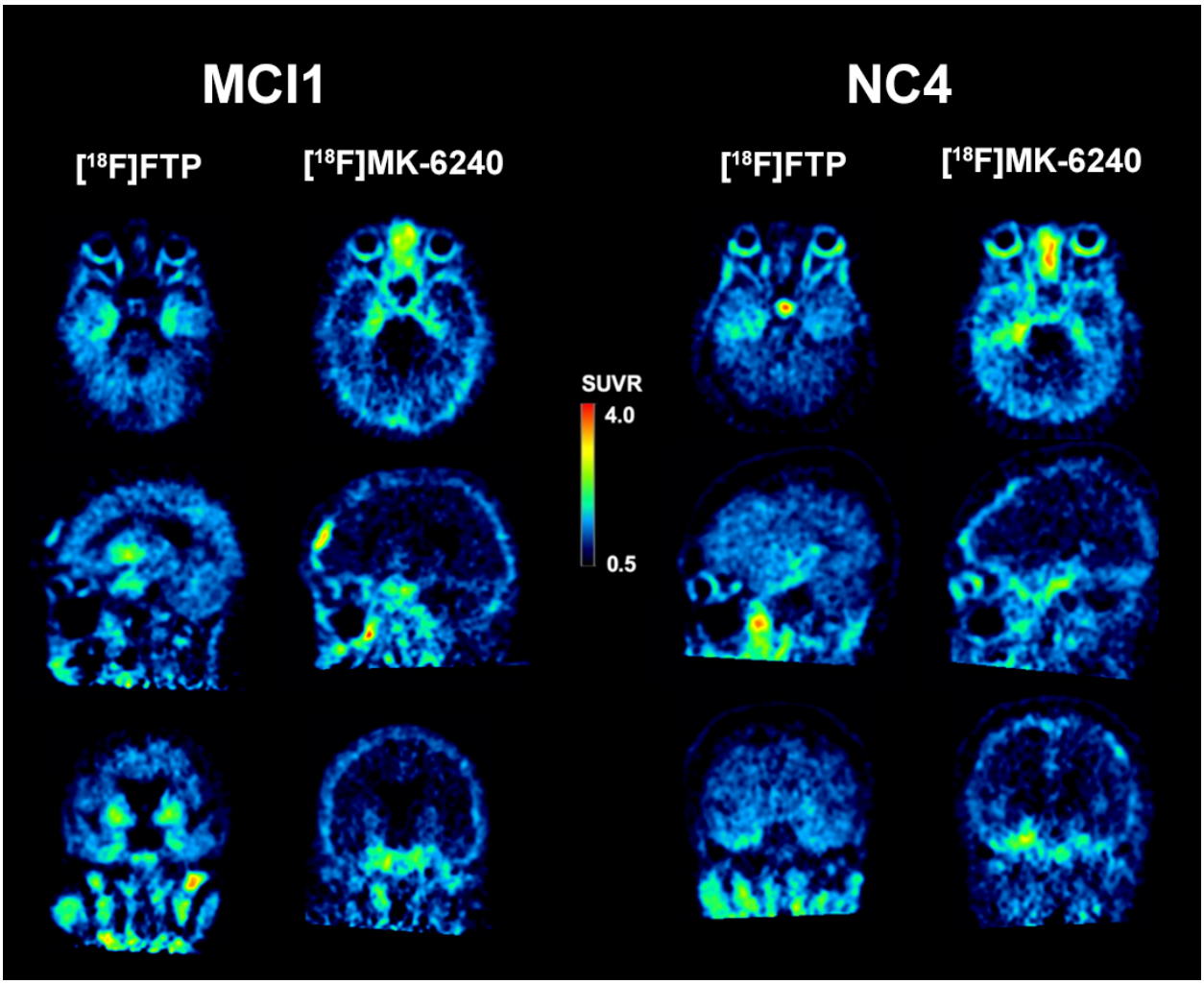

Supplementary Figure 4: Representative head-to-head transaxial (top row), sagittal (middle row) and coronal (bottom row) [^{18}F]flortaucipir ([^{18}F]FTP) and [^{18}F]MK-6240 for a healthy control (NC4, left) and an MCI participant (MCI1, right), showing the areas of non-concordant visual rating for 2 out of the 5 raters. NC4 illustrates the area of the discordant ratings in neocortex (majority "positive"), while MCI1 illustrates the area of reader disagreement in the MTL (majority "positive").